

# Copper Thiophosphate ( $\text{Cu}_3\text{PS}_4$ ) as an Electrode Material for Lithium Solid-State Batteries with Lithium Thiophosphate ( $\beta\text{-Li}_3\text{PS}_4$ ) Electrolyte

Zhenggang Zhang, Katherine A. Mazzio,\* Luise M. Riegger, Wolfgang Brehm, Jürgen Janek, Joachim Sann, and Philipp Adelhelm\*

Lithium thiophosphate ( $\beta\text{-Li}_3\text{PS}_4$ ) is a promising solid electrolyte (SE) for solid-state batteries (SSBs). A major limitation is its very narrow electrochemical stability window which is caused by redox reactions involving sulfur and phosphorous. As these redox processes can be reversible, thiophosphates can be also studied as electrode materials. Herein, the use of  $\text{Cu}_3\text{PS}_4$  as an active electrode material for Li SSBs with  $\beta\text{-Li}_3\text{PS}_4$  as the SE is explored. Both compounds exhibit similarities in crystal structure and composition which may benefit their compatibility. An In/InLi alloy is used as the counter electrode. The influence of electrode composition and temperature (room temperature and 60 °C) on the cell behavior is investigated. For an electrode composition of  $\text{Cu}_3\text{PS}_4$ :  $\beta\text{-Li}_3\text{PS}_4$ : C65 = 40: 50: 10 wt%, the initial discharge capacity at 60 °C is 776 mAh g<sup>-1</sup> which fades over 60 cycles to 508 mAh g<sup>-1</sup> when cycled between 0.8 and 2.8 V (vs. Li<sup>+</sup>/Li) at 50 mA g<sup>-1</sup> (254.8 μA cm<sup>-2</sup>). Analysis by X-ray diffraction and X-ray photoelectron spectroscopy shows that  $\text{Cu}_3\text{PS}_4$  irreversibly decomposes during lithiation. During cycling, the redox activity is found to be due to  $\text{Cu}_2\text{S}$  and  $\text{S}_8$  redox.

solids, a fact that is often emphasized by calling them all-solid-state batteries. Due to their solid nature, the performance of SSBs greatly depends on how fast the ions can travel within the solid electrolytes (SEs), how well the active materials (AMs) and SEs remain in contact during cycling, and whether the solid/solid interfaces between AMs and SEs are chemically stable.<sup>[2]</sup> Sulfide SEs (SSEs) such as  $\beta\text{-Li}_3\text{PS}_4$  are characterized as having high ionic conductivity and moderate mechanical strength, and are therefore widely used, especially when SSBs are prepared through simple cold pressing approaches and tested at room temperature.<sup>[3]</sup>

A limitation of SSEs is their narrow electrochemical stability window (ESW).  $\beta\text{-Li}_3\text{PS}_4$ , for example, has been calculated to only be stable between 1.71 and 2.31 V (vs. Li<sup>+</sup>/Li), so the SE easily reacts with the electrode materials.<sup>[2e]</sup> Kinetic

effects may increase the ESW, but the driving force for side reactions becomes greater the more the stability window is exceeded. High voltage cathode AMs (CAMs) with redox potentials > 4 V appear to be especially problematic.<sup>[2a]</sup> Stabilization of the electrode/SE interface by interphase formation or by coatings and dopants are prominent strategies to overcome this problem.<sup>[4]</sup>

## 1. Introduction

Solid-state batteries (SSBs) are attracting attention for their expected increased energy density and improved safety.<sup>[1]</sup> Compared to conventional lithium-ion batteries that are based on solid electrodes with liquid electrolyte, SSBs consist only of

Z. Zhang, K. A. Mazzio, P. Adelhelm  
Institut für Chemie  
Humboldt Universität zu Berlin  
12489 Berlin, Germany  
E-mail: katherine.mazzio@hu-berlin.de; philipp.adelhelm@hu-berlin.de

Z. Zhang  
Department of Materials Science and Engineering  
Southern University of Science and Technology  
Shenzhen 518055, China

 The ORCID identification number(s) for the author(s) of this article can be found under <https://doi.org/10.1002/ente.202300553>.

© 2023 The Authors. Energy Technology published by Wiley-VCH GmbH. This is an open access article under the terms of the Creative Commons Attribution License, which permits use, distribution and reproduction in any medium, provided the original work is properly cited.

DOI: 10.1002/ente.202300553

K. A. Mazzio, P. Adelhelm  
Helmholtz-Zentrum Berlin für Materialien und Energie  
Research Group Operando Battery Analysis (CE-COBA)  
14109 Berlin, Germany

L. M. Riegger, J. Janek, J. Sann  
Institute of Physical Chemistry  
Justus-Liebig-University Giessen  
35392 Giessen, Germany

W. Brehm  
Institut für Energie-und Automatisierungstechnik  
Technische Universität Berlin  
10587 Berlin, Germany

J. Janek, J. Sann  
Center for Materials Research (LaMa)  
Justus-Liebig-University Giessen  
35392 Giessen, Germany

Another mitigation strategy is to work with low-voltage CAMs that operate close to or within the ESW of the SEs. This leads to an undesired loss in cell voltage, but partial compensation can be achieved by using electrodes with specific capacities that significantly exceed those of conventional CAMs. This can be obtained through conversion reactions that typically provide capacity values in the range of several hundred mAh g<sup>-1</sup>.<sup>[5]</sup> While there are also challenges related to this approach, exploring the properties of conversion electrodes for SSBs is important. Conversion reactions can be classified into reactions with direct phase transformations or those that undergo decomposition reactions. Examples of the former include Li-S,<sup>[6]</sup> or Li alloys such as Li-Si,<sup>[7]</sup> Li-In,<sup>[8]</sup> or Li-Sn,<sup>[9]</sup> while the latter typically occur when Li (or Na) reacts with compounds such as M<sub>a</sub>X<sub>b</sub> (where M = Fe, Co, Ni, Cu, etc., and X = S, O, P, F, etc.). For example, various phosphides and sulfides such as NiP<sub>2</sub>,<sup>[10]</sup> Sn<sub>4</sub>P<sub>3</sub>,<sup>[11]</sup> FeS<sub>2</sub>,<sup>[12]</sup> Co<sub>9</sub>S<sub>8</sub>,<sup>[13]</sup> MoS<sub>2</sub>,<sup>[14]</sup> and CuS<sup>[15]</sup> have been studied as electrode materials for SSBs that are known to undergo decomposition reactions. More complex, e.g., ternary, compounds can of course undergo conversion reactions as well.

Considering their compositional and structural similarities, ternary compounds (M<sub>x</sub>P<sub>y</sub>S<sub>z</sub>, where M = Fe,<sup>[16]</sup> Ni, Co, Ag, Cu,<sup>[17]</sup> etc.) may form better interfaces with β-Li<sub>3</sub>PS<sub>4</sub> than binary M<sub>a</sub>X<sub>b</sub> compounds. However, their electrochemical properties have still been rarely studied in SSBs. Among the ternary compounds, FePS<sub>3</sub> has been investigated in SSBs. Fujiji et al. cycled this compound in a narrow stoichiometric window (< 200 mAh g<sup>-1</sup>) where only intercalation rather than conversion is believed to take place (formation of Li<sub>x</sub>FePS<sub>3</sub>).<sup>[16,18]</sup> Our group also investigated the use of Cu<sub>3</sub>PS<sub>4</sub> as an electrode material in Na-ion and Li-ion cells with liquid electrolytes.<sup>[17]</sup> While stable cycling was observed in Na-ion cells (> 1,000 cycles at about 450 mAh g<sup>-1</sup>), stronger fading occurred in Li-ion cells. The capacity degradation mechanism is

still not clear, but strong capacity fade is frequently observed in cells utilizing sulfur and metal sulfides as electrode materials.<sup>[19]</sup> The dissolution of polysulfide intermediates in liquid electrolytes and therefore loss of AM is considered the primary reason.<sup>[19b,20]</sup> In SSBs, such dissolution processes can be completely eliminated.

Herein, we utilize Cu<sub>3</sub>PS<sub>4</sub> as the AM with β-Li<sub>3</sub>PS<sub>4</sub> SE in SSBs. Cu<sub>3</sub>PS<sub>4</sub> was synthesized by ball milling and systematic studies on the electrochemical behavior were obtained by varying the cathode composition (Cu<sub>3</sub>PS<sub>4</sub>: β-Li<sub>3</sub>PS<sub>4</sub>: C65 = 40: 50: 10 wt% or 60: 30: 10 wt%, labeled throughout as 451 and 631, respectively) and the temperature (room temperature [RT] and 60 °C). We found that both the working temperature and the cathode composition play an important role in the battery performance. We subsequently investigated the reaction mechanism of Cu<sub>3</sub>PS<sub>4</sub> using X-ray diffraction (XRD), X-ray photoelectron spectroscopy (XPS), and Raman spectroscopy.

## 2. Results and Discussion

Cu<sub>3</sub>PS<sub>4</sub> was synthesized by ball milling and characterized by XRD, scanning electron microscopy (SEM), and energy-dispersive X-ray spectroscopy (EDX), as shown in **Figure 1**. The XRD pattern shows that the synthesized Cu<sub>3</sub>PS<sub>4</sub> has a crystal structure that is orthorhombic with a *Pmn*21 space group, which matches that of the Cu<sub>3</sub>PS<sub>4</sub> reference pattern (ICSD 98-041-2240). The relatively wide peaks indicate a small average crystallite size. SEM images of the sample show that the prepared Cu<sub>3</sub>PS<sub>4</sub> particles have a large size distribution, with agglomerates up to 10 μm in diameter and with highly roughened surfaces. According to EDX analysis, Cu, P, and S are homogeneously distributed without isolated regions of enhanced stoichiometry.

In this experiment, the theoretical conversion reaction of the Cu<sub>3</sub>PS<sub>4</sub> with Li is expected to be

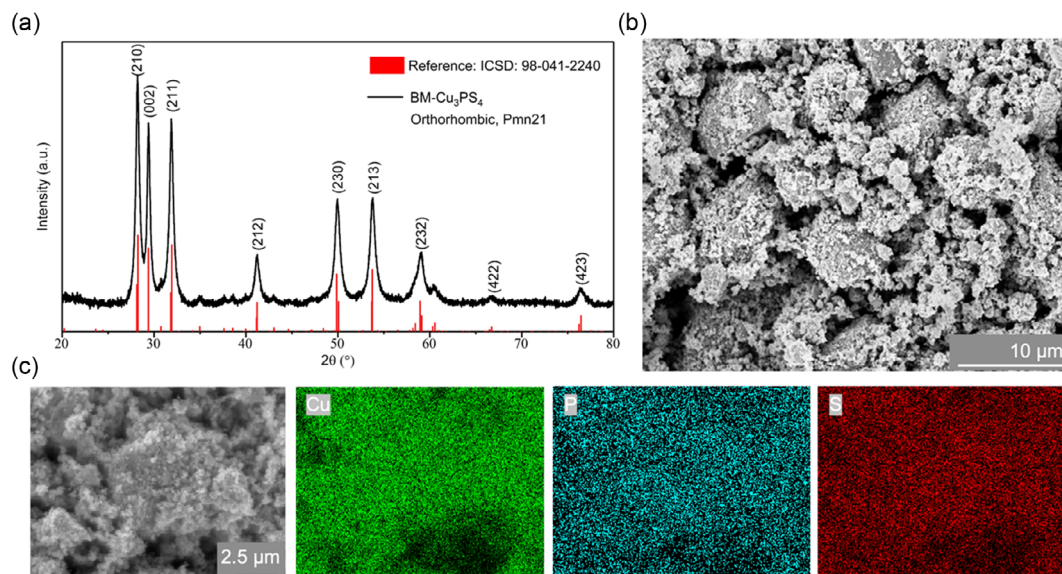
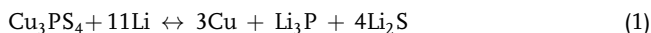


**Figure 1.** Structural and morphological characterization of the synthesized Cu<sub>3</sub>PS<sub>4</sub>. a) X-ray diffraction (XRD) pattern of Cu<sub>3</sub>PS<sub>4</sub> prepared by ball milling alongside the Cu<sub>3</sub>PS<sub>4</sub> reference pattern (ICSD 98-041-2240). b) SEM image of the Cu<sub>3</sub>PS<sub>4</sub> powder. The scale bar is 10 μm. c) SEM image of the Cu<sub>3</sub>PS<sub>4</sub> powder with Cu, P, and S elemental mapping by EDX. The scale bar is 2.5 μm.



Properties of  $\text{Cu}_3\text{PS}_4$  have been calculated based on the aforementioned reaction and the results are presented in **Table 1**. The calculated theoretical energy density of the reaction and the capacity of  $\text{Cu}_3\text{PS}_4$  were determined to be  $1301.5 \text{ Wh kg}^{-1}$  ( $5392.1 \text{ Wh L}^{-1}$ ) and  $843 \text{ mAh g}^{-1}$  ( $3492.5 \text{ mAh cm}^{-3}$ ). Taking the volumes of  $\text{Cu}_3\text{PS}_4$  and the products (Cu,  $\text{Li}_3\text{P}$ , and  $\text{Li}_2\text{S}$ ) into account,  $\text{Cu}_3\text{PS}_4$  can be expected to expand by 53.9% during the conversion reaction in accordance with Equation (2) (cell volume values from ICSD for  $\text{Cu}_3\text{PS}_4$ , Cu,  $\text{Li}_3\text{P}$ , and  $\text{Li}_2\text{S}$  are 278.7, 48.8, 117.6, and  $119.0 \text{ \AA}^3$ , respectively).

$$\Delta V_{\text{AM}} = [(V_{\text{product}} - V_{\text{reactant}}) \div V_{\text{reactant}}] \times 100\% \quad (2)$$

Such a large volume expansion and the formation of compounds with very different structures (Cu,  $\text{Li}_3\text{P}$ , and  $\text{Li}_2\text{S}$ ) can easily lead to crack formation in the cathode of the SSBs. Note that the relative change is smaller when including the volume of the SE and the conductive additive (+12.2% for 451 and +21.2% for 631) and even less when porosity is included. Nevertheless, maintaining good contact during cycling appears more challenging when compared to standard cathode materials such as NMC, which typically show volume changes below 10% on the materials basis and at the same time maintain their crystal structure. It is also worthwhile to note that while the cathode expands during discharge, the anode volume decreases. The different volume changes in the SSBs lead to a quite dynamic behavior which can be followed in situ by tomography as has been shown for the conversion reaction of Li with  $\text{CuS}$ .<sup>[15c]</sup>

Beyond the cell reaction itself, some excess capacity can be obtained due to the limited ESW of  $\beta\text{-Li}_3\text{PS}_4$ . In particular, the carbon conductive additive can trigger these types of reactions.<sup>[21]</sup> To estimate the capacity contributions arising from  $\beta\text{-Li}_3\text{PS}_4$  and Super C65 conductive carbon black (C65), an SSB without  $\text{Cu}_3\text{PS}_4$  was studied by taking  $\beta\text{-Li}_3\text{PS}_4$  as the electrode material ( $\beta\text{-Li}_3\text{PS}_4$ : C65 = 3: 1 wt%), see Figure S1, Supporting Information. The initial discharge and charge capacities were 109 and  $31 \text{ mAh g}^{-1}$ , respectively, after which the cell approached a reversible capacity of  $28 \text{ mAh g}^{-1}$ . As the carbon additive does not contribute to the capacity, the assumed

**Table 1.** Properties of the ideal theoretical conversion reaction of  $\text{Cu}_3\text{PS}_4$  with Li.

$w_{\text{th}}$ ( $\text{Cu}_3\text{PS}_4$ ) by weight in $\text{Wh kg}^{-1}$	1301.5 <sup>a)</sup>
$W_{\text{th}}$ ( $\text{Cu}_3\text{PS}_4$ ) by volume in $\text{Wh L}^{-1}$	5392.1
$E_{\text{th}}$ ( $\text{Cu}_3\text{PS}_4$ ) in V	1.544
$q_{\text{th}}$ ( $\text{Cu}_3\text{PS}_4$ ) by weight in $\text{mAh g}^{-1}$	843
$Q_{\text{th}}$ ( $\text{Cu}_3\text{PS}_4$ ) by volume in $\text{mAh cm}^{-3}$	3492.5
Number of transferred electrons	11
Volume change w.r.t. $\text{Cu}_3\text{PS}_4$ /%	+53.9
Volume expansion of $\text{Cu}_3\text{PS}_4$ electrode/%	+12.2 (40: 50: 10 wt%)/ + 21.2 (60: 30: 10 wt%) <sup>b)</sup>

<sup>a)</sup>  $\Delta_f G_{\text{Li}_2\text{S}} = -432 \text{ kJ/mol}$ ;  $\Delta_f G_{\text{Li}_3\text{P}} = -312.366 \text{ kJ/mol}$ ;  $\Delta_f G_{\text{Cu}_3\text{PS}_4} \approx \Delta_f H_{\text{Cu}_3\text{PS}_4} = -401.529 \text{ kJ/mol}$ . <sup>b)</sup> The volume change was calculated based on the  $\text{Cu}_3\text{PS}_4$  without considering the influence of  $\beta\text{-Li}_3\text{PS}_4$  and C65.

excess capacity of the SE amounts to  $28 \text{ mAh g}^{-1}[\beta\text{-Li}_3\text{PS}_4]$ . Considering the capacity that originates from the side reactions between C65 and  $\beta\text{-Li}_3\text{PS}_4$  (Figure S1, Supporting Information), the mass/volume loading of C65 was held constant at a mass of 1 mg in the 10 mg cathode composites for both the 451 and 631 cases.

## 3. Electrochemical Properties

### 3.1. Cathode Composition

It is well known that the composition of the cathode composite has a strong influence on its electrochemical behavior. While maximizing the content of CAMs ( $\text{Cu}_3\text{PS}_4$ ) is desirable, sufficient amounts of SE ( $\beta\text{-Li}_3\text{PS}_4$ ) and conductive additive (C65) are necessary to provide sufficient electronic and ionic conducting pathways. For the general electrode composition  $\text{Cu}_3\text{PS}_4$ :  $\beta\text{-Li}_3\text{PS}_4$ : C65, two different compositions with contents of 40: 50: 10 wt% (451) and 60: 30: 10 wt% (631) were studied. Assuming full conversion, the theoretical areal capacities amount to  $4.30 \text{ mAh cm}^{-2}$  (451) and  $6.49 \text{ mAh cm}^{-2}$  (631).  $\beta\text{-Li}_3\text{PS}_4$  also served as a separator electrolyte and an In/InLi two-phase mixture was used as the counter electrode. Note that the cell voltage refers to a Li counter electrode, i.e., all measured values were shifted by 0.62 V.<sup>[8]</sup> The capacity and current were calculated using the weight of  $\text{Cu}_3\text{PS}_4$  in the electrode. Details of the cathode compositions are displayed in **Figure 2**.

For activation of the electrodes, the SSBs were first cycled at low currents over 5 cycles while subsequently increasing the voltage window. This was done at  $10 \text{ mA g}^{-1}$  between 1.0 and 2.8 V (2 cycles), between 0.9 and 2.8 V (2 cycles), and between 0.8 and 2.8 V (1 cycle).<sup>[22]</sup> After this pre-cycling, the cycle life tests were performed at  $50 \text{ mA g}^{-1}$  between 0.8 and 2.8 V. Unless otherwise specified, all electrochemical properties were measured at RT.

Charge/discharge curves of the first cycle (1.0–2.8 V at  $10 \text{ mA g}^{-1}$ ) are depicted in **Figure 3a** and show the expected complex behavior. During discharging, the electrode with the higher SE content (451) shows a higher discharge capacity due to a more elongated lower voltage plateau. The 451 electrode also shows a higher charging capacity and more defined voltage plateaus compared to the 631 electrode. The difference between the electrodes can be more clearly seen from hysteresis and  $dQ/dV$  plots, see Figure S2, Supporting Information. Values for the specific capacities at the end of the first cycle reach  $328 \text{ mAh g}^{-1}$  for the 631 battery and  $699 \text{ mAh g}^{-1}$  for the 451 battery. A comparison of the voltage profiles shows that the lower capacity of the 631 electrode is due to a stronger polarization, i.e., the cutoff potentials are reached earlier. Both cells are rechargeable but the initial Coulomb efficiency (ICE) of 114% for the 451 cell indicates the presence of some side reactions. Changes in the voltage profiles after multiple cycles can be seen in **Figure 3b** where the voltage profiles of the 10th and 60th cycles are compared. Relative to the first cycle, the low-voltage plateau around 1.1 V versus  $\text{Li}^+/\text{Li}$  has disappeared but an additional step slightly below 2.0 V appears. This step is clearly visible for the 451 cell (see also Figure S2, Supporting Information) and indicates a change in the reaction mechanism, which is discussed later. Values for the specific discharge capacities and Coulomb efficiencies

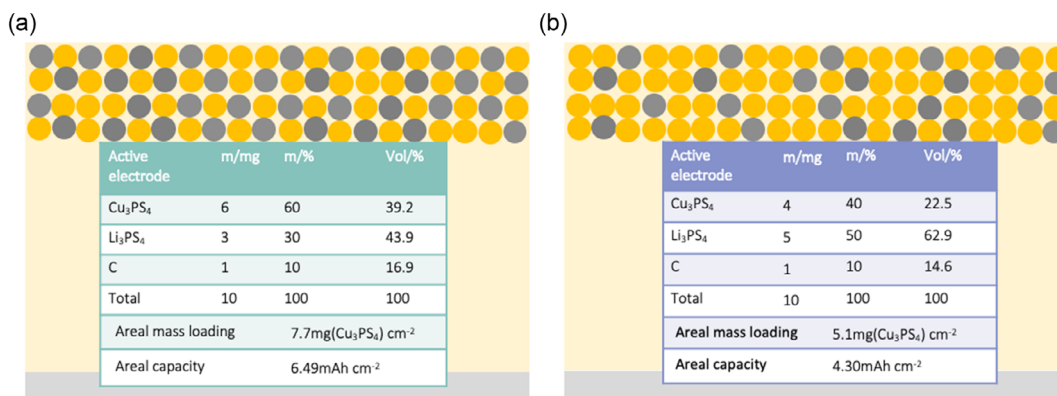


**Figure 2.** For simplicity, Cu<sub>3</sub>PS<sub>4</sub> (grey) and β-Li<sub>3</sub>PS<sub>4</sub> (gold) are shown as round particles and the conductive additive C65 is neglected. The details of the a) 631 and b) 451 electrodes are shown in the inserted tables. The volume ratios are derived by taking the corresponding bulk densities of Cu<sub>3</sub>PS<sub>4</sub>, β-Li<sub>3</sub>PS<sub>4</sub>, and C65 as 4.14 (HighScore), 1.85 (HighScore), and 1.60 (MSE Supplies) g cm<sup>-3</sup>, respectively.

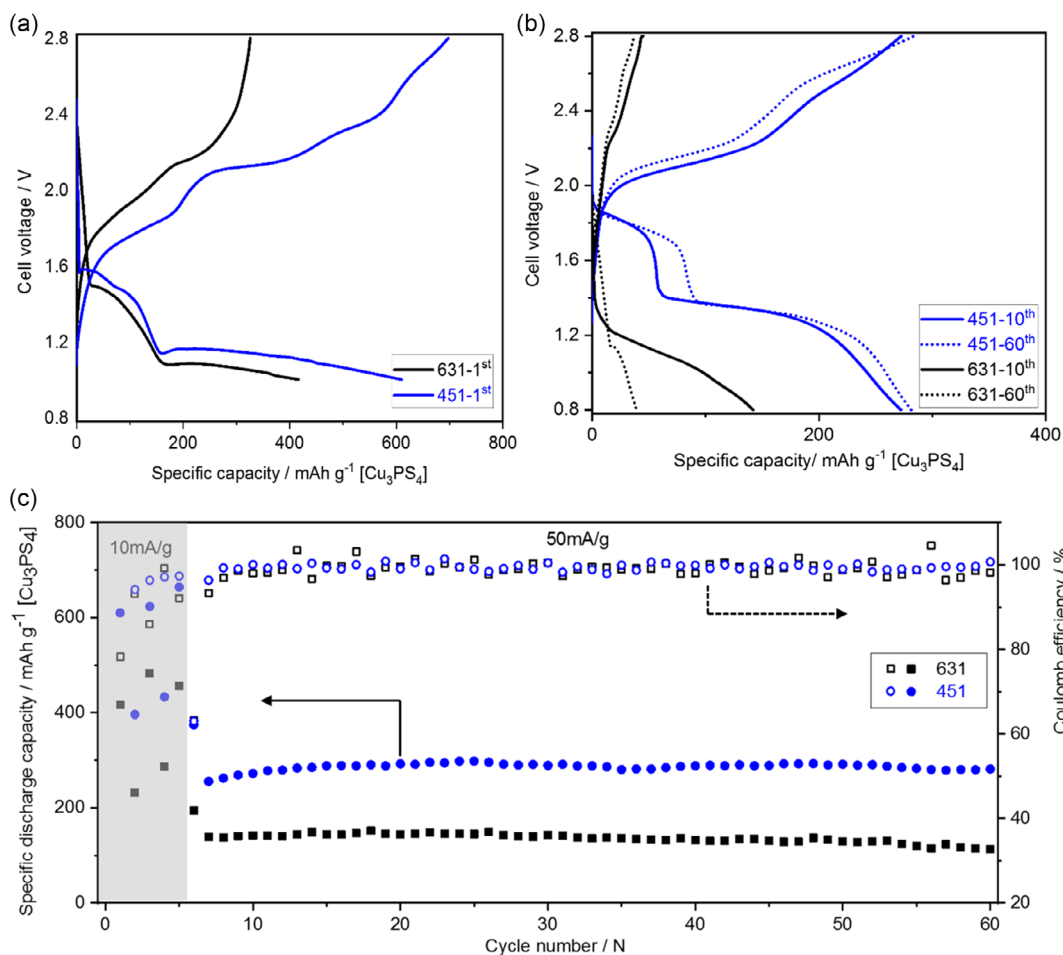


**Figure 3.** Cycling performance of the 451 (blue) and 631 (black) solid-state batteries (SSBs) at room temperature (RT). a) The 1st charge–discharge voltage profiles of In/InLi|β-Li<sub>3</sub>PS<sub>4</sub>|[Cu<sub>3</sub>PS<sub>4</sub>: β-Li<sub>3</sub>PS<sub>4</sub>: C65] batteries between 1.0 and 2.8 V. b) The charge–discharge voltage profiles for the 10th and 60th cycles at 50 mA g<sup>-1</sup> between 0.8 and 2.8 V. c) The specific discharge capacity (filled circles) and Coulomb efficiency (CE) (open circles) during cycling. The pre-cycling section is highlighted in the grey box.

(CEs) over 60 cycles are shown in Figure 3c. At the increased current density of  $50 \text{ mA g}^{-1}$ , capacity values of  $140 \text{ mAh g}^{-1}$  and  $290 \text{ mAh g}^{-1}$  are reached for the 631 and 451 cell, respectively. These values remain stable over 60 cycles, with CE values close to 100%, indicating a reversible electrode reaction.

Overall, the SSBs with  $\text{Cu}_3\text{PS}_4$  as CAM could be successfully cycled and stable capacity values were obtained. Large polarization was observed and capacities were clearly below the theoretical value of  $843 \text{ mAh g}^{-1}$ . Nevertheless, stable values close to 300 at  $50 \text{ mA g}^{-1}$  could be reached for the 451 cell between 0.8 and 2.8 V. This corresponds to an areal capacity of about  $1.5 \text{ mAh cm}^{-2}$ . Compared to this, the 631 cell showed inferior behavior. Further optimization of electrode parameters can lead to improved behavior, but this is outside the scope of this study. Due to the higher capacity, all further measurements were done using the 451 composition.

### 3.2. Effect of Temperature

An approach to mitigate the strong electrode polarization is to increase the cell temperature, as many processes such as ionic conduction or chemical reactions are governed by Arrhenius

relationships. **Figure 4** compares the voltage profile of the 451 cell at RT and at  $60^\circ\text{C}$  (high temperature, HT).

Figure 4a shows the initial voltage profiles at both temperatures. Similar discharge and charge capacities are observed although the upper voltage plateau around 2.1 V appears larger at  $60^\circ\text{C}$ . The slightly lower capacity at HT seems to be rooted in the smaller lower voltage plateau around 1.1 V, leading to a slightly earlier end of discharge. In both cases, the ICE value exceeds 100% to a similar degree (114% at RT and 118% at HT). Corresponding hysteresis plots and derivative plots can be found in Figure S3, Supporting Information. The beneficial effect of higher temperature becomes more evident during the following cycles, as can be seen from Figure 4b,c. Figure 4b shows the voltage profiles for the 10th and 60th cycles for which much higher capacities are observed at HT. The discharge profiles show two steps but they are more defined and larger at HT. The voltage hysteresis also becomes smaller at HT, indicating that kinetic effects limited the electrode reaction. During cycling over 60 cycles, the capacity at HT is about  $200 \text{ mAh g}^{-1}$  larger compared to RT, though a faster degradation seems to set in after about 35 cycles. After 60 cycles, the capacity at HT is close to  $500 \text{ mAh g}^{-1}$  which corresponds to 59% of the theoretical

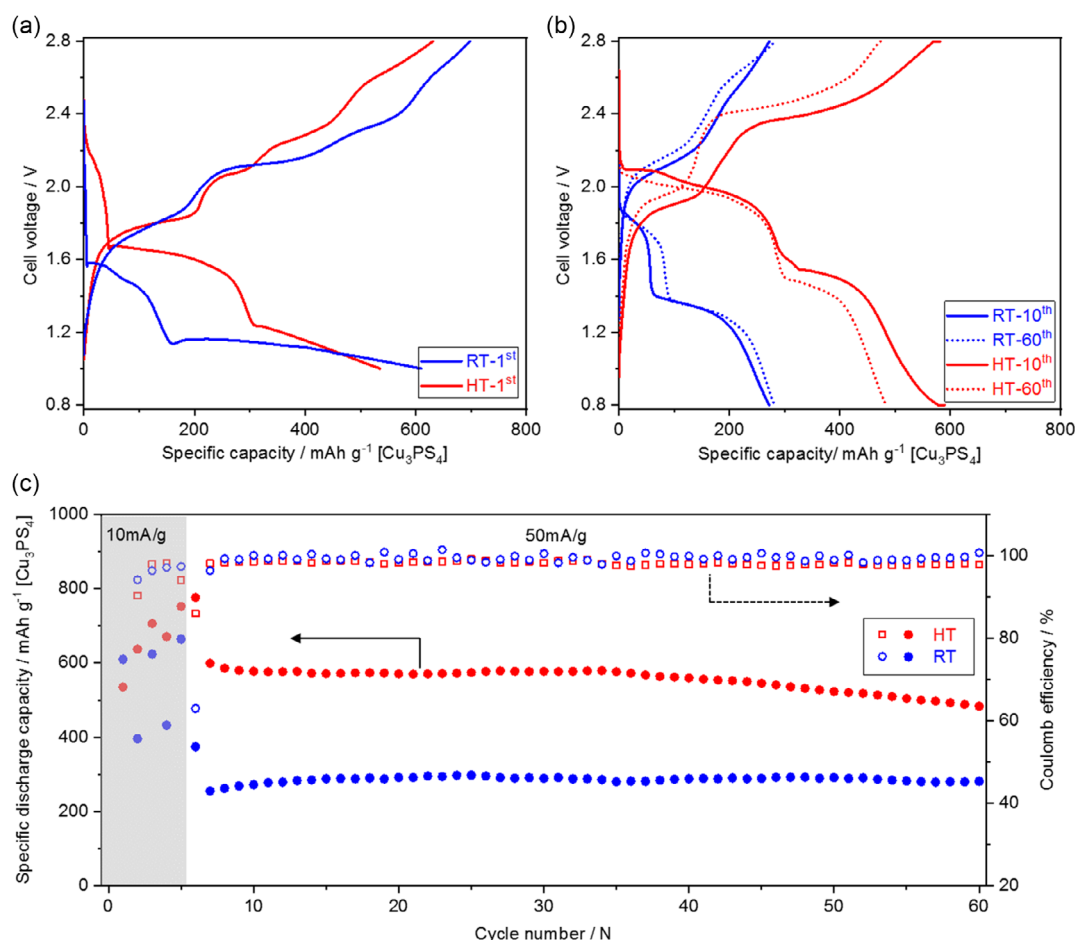


**Figure 4.** Cycling performance of the 451 SSBs at RT (blue) and high temperature (HT) (red). a) The 1st charge–discharge voltage profiles of  $\text{In}/\text{InLi}/\beta\text{-Li}_3\text{PS}_4/\text{Cu}_3\text{PS}_4/\beta\text{-Li}_3\text{PS}_4/\text{C65}$  (451) in the voltage range between 1.0 and 2.8 V at  $10 \text{ mA g}^{-1}$ . b) The 10th and 60th cycles at  $50 \text{ mA g}^{-1}$  between 0.8 and 2.8 V. c) The overall cycling stability (filled circles) and CE (open circles) during cycling. The pre-cycling section is highlighted in the grey box.

capacity (or  $2.55 \text{ mAh cm}^{-2}$ ). As this is a clear improvement compared to RT, the analytical studies in the next sections were performed on 451 samples that were cycled at  $60^\circ\text{C}$ .

### 3.3. Reaction Mechanism

The low capacity of the electrodes compared to the theoretical value along with clear changes in the voltage profile between the first and later cycles indicate that the reaction mechanism is different from what is expected from Equation (1). The multiple steps in the voltage profile also indicate that there are several redox active species. Conversion reactions are generally difficult to characterize due to amorphization and the appearance of intermediate phases. This becomes even more challenging in SSBs because their constituent layers (anode, electrolyte, cathode) cannot be easily dismantled and at the same time, the SE amounts to a large fraction of the cathode. Here, we used postmortem XRD, XPS, and Raman spectroscopy to elucidate the reaction mechanism of  $\text{Cu}_3\text{PS}_4$  in SSBs.

#### 3.3.1. XRD Analysis

Figure 5 shows XRD patterns of the electrodes at different states of charge. At open circuit voltage (OCV), see Figure 5b(I), the electrodes show crystal structures consistent with the expected combination of  $\text{Cu}_3\text{PS}_4$  and  $\beta\text{-Li}_3\text{PS}_4$ . Upon discharging to 1.4 V (Figure 5b(II)),  $\text{Cu}_3\text{PS}_4$  is still visible and there are the first indications of crystalline reaction products with a new signal beginning to arise at  $26.8^\circ$  ( $2\theta$ ). This most likely corresponds to the high intensity (111) peak from  $\text{Li}_2\text{S}$  in an anti-fluorite crystal structure with  $\text{Fm}\bar{3}\text{m}$  space group. This feature

was first observed after nearly 2.35 formula units of Li reacted per formula unit of  $\text{Cu}_3\text{PS}_4$ . In our previous study focused on sodium-ion batteries using  $\text{Cu}_3\text{PS}_4$  as the AM, we found that the  $\text{Cu}_3\text{PS}_4$  gradually converted to a combination of Cu and  $\text{Na}_2\text{S}$  after sodiation commenced, which we used to demonstrate that  $\text{Cu}_3\text{PS}_4$  reacts in a conversion-type mechanism with sodium.<sup>[17]</sup> In this case, there is some evidence for the possibility of  $\text{Li}_2\text{S}$  formation after the cell was discharged to 1.4 V, but the concomitant presence of elemental Cu in the electrode at this stage is not clear and further analysis is necessary to confirm, as discussed later. According to Xu et al., a fast ion-conducting, thermodynamically stable intermediate compound  $\text{Li}_2\text{CuPS}_4$  exists in the Cu–P–S–Li quaternary phase diagram.<sup>[23]</sup> Favored by the similar  $\text{Li}^+$  and  $\text{Cu}^+$  ionic radii (similarity >98%), a displacement reaction could take place during the early lithiation period. While we do not observe the presence of a new crystalline species by XRD, further characterization is necessary to understand if  $\text{Li}_2\text{CuPS}_4$  or a related compound is present in an amorphous or metastable state. Upon discharge to 0.8 V (Figure 5b(III)), it can be seen that the conversion mechanism has occurred due to the clear formation of  $\text{Li}_2\text{S}$  with the (111), (220), and (311) reflections at  $26.8^\circ$ ,  $44.5^\circ$ , and  $52.7^\circ$  ( $2\theta$ ) and Cu ( $\text{Fm}\bar{3}\text{m}$  space group) with the (111) and (200) reflections at  $43.0^\circ$  and  $52.6^\circ$  ( $2\theta$ ). At the same time, reflections from  $\text{Cu}_3\text{PS}_4$  are no longer visible. Upon charging to 1.9 V (Figure 5b(IV)), it can be clearly seen that the relative intensity ratio between the identified Cu and  $\text{Li}_2\text{S}$  reflections changes, as indicated by the relative decrease in Cu (111) at  $43.0^\circ$  ( $2\theta$ ). Cu is expected to undergo an oxidation reaction during charge, while  $\text{Li}^+$  from the  $\text{Li}_2\text{S}$  should be reduced at the anode. Correspondingly, we can consider that the relatively strong

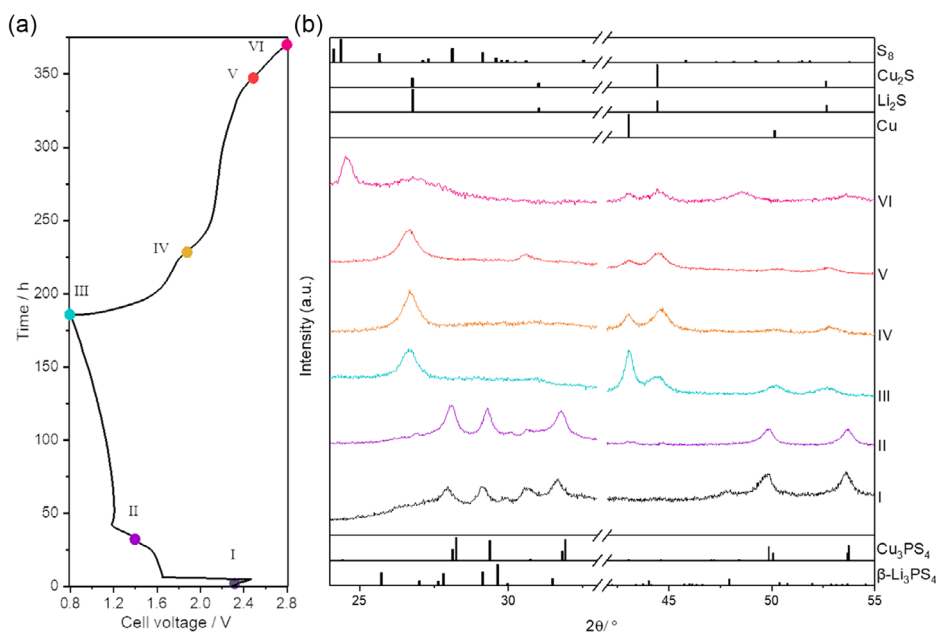


**Figure 5.** Postmortem XRD results of the 451 HT SSB. a) A voltage profile at  $5 \text{ mA g}^{-1}$  highlighting the specific states of charge marked as I–VI where ex situ XRD measurements were performed. I: OCV state, II: discharged to 1.4 V, III: discharged to 0.8 V, IV: charged to 1.9 V, V: charged to 2.5 V, and VI: charged to 2.8 V. b) The XRD patterns of the electrodes measured at the corresponding specific states of charge. The reference patterns for initial reactants (bottom) and products (top) were obtained from the ICSD:  $\text{Cu}_3\text{PS}_4$  (98-041-2240),  $\text{Li}_2\text{S}$  (blue, 98-005-4396), Cu (green, 98-018-0109),  $\text{Cu}_2\text{S}$  (orange, 98-009-5398), and S (98-008-2372).

reflections previously associated with  $\text{Li}_2\text{S}$  now correspond to a combination of residual  $\text{Li}_2\text{S}$  with  $\text{Cu}_2\text{S}$ . The reflections are expected to strongly overlap due to the similar crystal structure and ionic radii of  $\text{Li}^+$  and  $\text{Cu}^+$ . This is further supported *vide infra* with XPS analysis. Consequently, the fractions of  $\text{Cu}_2\text{S}$  and  $\text{Cu} + \text{Li}_2\text{S}$  in the electrode behave in an opposite manner. This is observed to continue with greater charging to 2.5 V (Figure 5b(V)). However, after charging to 2.8 V (Figure 5b(VI)), the Cu is not observed to be fully consumed, as can be seen by the XRD signal at  $43.0^\circ$  ( $2\theta$ ). It is not feasible to quantify the amount of  $\text{Cu}_2\text{S}$  and  $\text{Li}_2\text{S}$  from XRD because their signals strongly overlap with each other. A new peak is also observed at  $24.5^\circ$  ( $2\theta$ ) after fully charging to 2.8 V, which can be ascribed to the appearance of sulfur ( $\text{S}_8$ ) in the  $\gamma$ -phase (P12/c1). This statement is in line with the literature which has shown that metal sulfides and  $\text{S}_8$  can form when  $\text{Li}_2\text{S}$  is well mixed with transition metals like Cu.<sup>[24]</sup>

Based on the XRD results, it appears that the  $\text{Cu}_3\text{PS}_4$  reacts in a different way with lithium than with sodium. The pristine  $\text{Cu}_3\text{PS}_4$  is converted to Cu and  $\text{Li}_2\text{S}$  after discharge. Furthermore, the reaction proceeds in an irreversible manner, as shown by the presence of not only residual Cu and  $\text{Li}_2\text{S}$ , but also  $\text{Cu}_2\text{S}$  and  $\text{S}_8$  in the electrode after charging. We were unable to identify the state of phosphorus-containing products after OCV by XRD and there is also the possibility of other amorphous products being formed during cycling. Therefore, additional analytical tools including XPS and Raman spectroscopy were employed in this study to identify the development of additional phases and support the XRD results.

### 3.3.2. XPS Analysis

XPS was used as a complimentary technique to XRD that provides information on the chemical composition and oxidation state of elements in the electrode that is also capable of analysis of materials in the amorphous state. Due to decomposition of the SE at the current collector during cycling, depth profiles were measured to study the decomposition of the CAM|SE interface for electrodes with a composition of  $\text{Cu}_3\text{PS}_4$ :  $\beta\text{-Li}_3\text{PS}_4$ : C65 = 40: 50: 10 wt%.<sup>[25]</sup> Here, 16 min of sputtering was chosen, as the spectra were found to not change further with additional sputtering time. Therefore, we assume that the influence of the current collector on these spectra is negligible and that the spectra represent the bulk of the catholyte. Furthermore, possible effects arising from any unintended water or oxygen exposure are minimized. The spectra were shifted with reference to  $\text{PS}_4^{3-}$  peaks at 161.8 eV (S  $2p_{3/2}$ ) and 132.1 eV (P  $2p_{3/2}$ ) in the S2p and P2p spectra, respectively.<sup>[25b,26]</sup>

X-ray photoelectron (XP) spectra for the S2p, P2p, and Cu2p of pristine  $\beta\text{-Li}_3\text{PS}_4$ ,  $\text{Cu}_3\text{PS}_4$ , and electrodes cycled to different states of charge are shown in Figure 6a. The pristine  $\beta\text{-Li}_3\text{PS}_4$  spectrum consists predominantly of  $\text{PS}_4^{3-}$  (blue) with signals at 161.8 and 132.1 eV for the S2p and P2p spectra, respectively. Impurities at higher binding energies (S  $2p_{3/2}$  at 163.2 eV and P  $2p_{3/2}$  at 132.9 eV) are also observed that can be assigned to P-[S]<sub>n</sub>-P anionic frameworks (purple). It is known that intermediate P-[S]<sub>n</sub>-P anionic structures like  $\text{P}_2\text{S}_6^{4-}$  and  $\text{P}_2\text{S}_6^{2-}$  can form when  $\text{PS}_4^{3-}$  converts to  $\text{P}_2\text{S}_5$ .<sup>[21b,24d,25a,27]</sup> At the same time, these P-[S]<sub>n</sub>-P intermediates can readily oxidize to  $\text{PO}_4^{3-}/\text{P}_2\text{O}_7^{4-}$  when

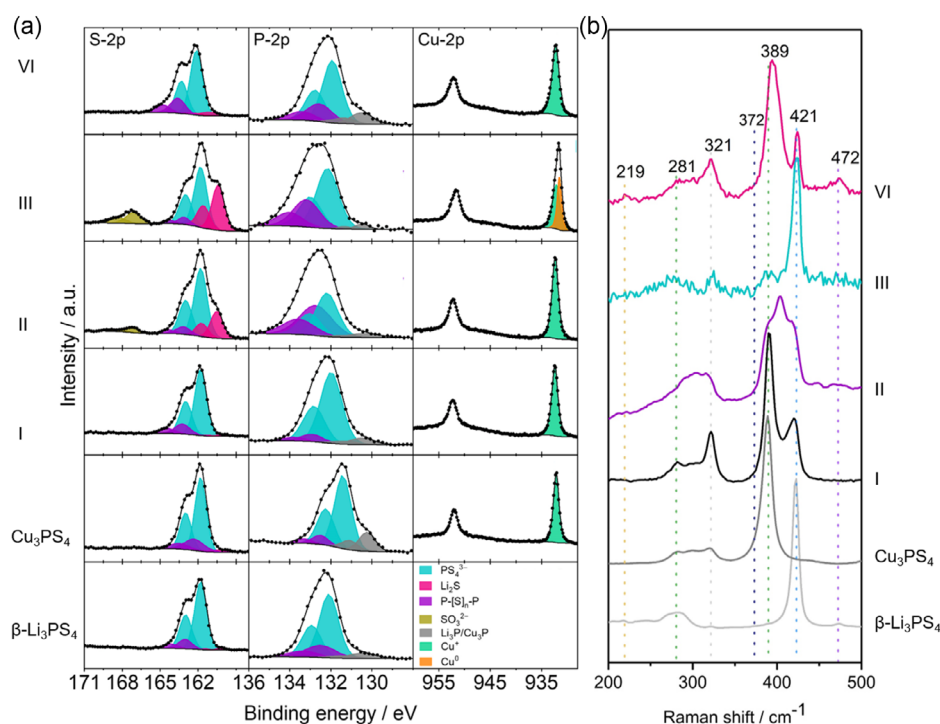


**Figure 6.** Postmortem X-ray photoelectron spectroscopy (XPS) and Raman spectroscopies. a) S2p, P2p, and Cu2p XPS; and b) Raman spectra of the electrode at I: OCV state; II: discharged to 1.4 V; III: discharged to 0.8 V; and VI: charged to 2.8 V. The XPS peaks were normalized to the S2p  $\text{PS}_4^{3-}$  signal at 161.8 eV, while the Raman data were normalized to the highest intensity peak of each spectrum.

exposed to oxygen.<sup>[28]</sup> In the P2*p* signal of  $\beta$ -Li<sub>3</sub>PS<sub>4</sub>, there is also a low BE peak observed that may be attributable to the presence of phosphorous in a reduced state (possibly P<sup>3+</sup>, grey, P 2*p*<sub>3/2</sub> at 131.0 eV).<sup>[29]</sup> Additionally, a minor signal assigned to Li<sub>2</sub>S can be found in the S2*p* spectrum at 160.2 eV. For Cu<sub>3</sub>PS<sub>4</sub>, the S2*p* and P2*p* XP spectra are similar to those of  $\beta$ -Li<sub>3</sub>PS<sub>4</sub>, but with a shift in the P 2*p*<sub>3/2</sub> peaks to lower BE at 131.4 eV, which is caused by the different electronegativities of Cu<sup>+</sup> and Li<sup>+</sup>. The Cu<sup>+</sup> has a peak at 932.3 eV in the Cu2*p* spectrum and the Cu LMM line has a BE of 570 eV (Figure S4, Supporting Information).

Upon discharging to 1.4 V (Figure 6a(II)), the Li<sub>2</sub>S signal intensity increases (S 2*p*<sub>3/2</sub> at 160.5 eV) confirming the XRD measurement results. An additional signal arises at higher BE (S 2*p*<sub>3/2</sub> at 167.1 eV) which is assigned to SO<sub>3</sub><sup>2-</sup> formation.<sup>[30]</sup> The SO<sub>3</sub><sup>2-</sup> might be caused by oxygen or water contamination during sample preparation. Also, the P2*p* peak at 132.8 eV is significantly larger than for the sample under OCV conditions. This indicates that the phosphorous has also reacted with oxygen or water and that oxygenated phosphorous species, such as phosphates, metaphosphates, or PS<sub>4-x</sub>O<sub>x</sub><sup>3-</sup>, were formed.<sup>[25b,31]</sup> The Cu 2*p* spectrum looks similar to that of the OCV state (Cu 2*p*<sub>3/2</sub> at 932.3 eV) and no satellites that would indicate Cu<sup>2+</sup> species can be detected. Therefore, we conclude that the oxidation state of Cu remains +1. Unfortunately, the Cu2*p* binding energies of Cu<sub>3</sub>PS<sub>4</sub>, Cu<sub>2</sub>S, and Cu<sub>3</sub>P are similar,<sup>[32]</sup> thus identification of the chemical composition is not possible by XPS. However, no Cu<sup>0</sup> signal was found at this voltage, which is confirmed by the Cu LMM spectrum. This further supports that the Cu<sub>3</sub>PS<sub>4</sub> reacts according to a different mechanism in lithium than in sodium in the early discharge period.

When further discharged to 0.8 V (Figure 6a(III)), Cu<sup>0</sup> is observed to form by the presence of an additional Cu 2*p*<sub>3/2</sub> peak at 931.6 eV and Cu LMM at 567 eV (see Figure S4(III), Supporting Information), which supports the XRD data. However, the Cu<sup>0</sup> is observed alongside a significant fraction of Cu<sup>+</sup>, showing that not all the Cu<sup>+</sup> is thoroughly reduced to Cu<sup>0</sup> at 0.8 V vs. Li<sup>+</sup>/Li. While the Li<sub>2</sub>S concentration increases upon reduction, no increase can be measured for the reduced phosphorous species. Thus, both XRD and XPS measurements are unable to confirm the formation of Li<sub>3</sub>P. As with the sample stopped at 1.4 V, SO<sub>3</sub><sup>2-</sup> signals (167.1 eV) and an increased P2*p* signal at 133.2 eV were found as well, indicating side reactions with oxygen and water.

Upon subsequent charging to 2.8 V (Figure 6a(VI)), the Cu 2*p* and Cu LMM spectra show that all Cu<sup>0</sup> has been oxidized back to Cu<sup>+</sup>. At the same time, the S 2*p* spectrum indicates that only a small fraction of residual Li<sub>2</sub>S remains. This indicates that the XRD features at 26.8° and 44.4° (2θ) (see Figure 4b(VI)) arise from Cu<sub>2</sub>S and not Li<sub>2</sub>S. No S<sub>8</sub> signals were detected in the S2*p* XPS spectrum after charging, which can occur due to evaporation of sulfur under UHV conditions.<sup>[33]</sup>

The XPS results demonstrate that the Cu<sub>3</sub>PS<sub>4</sub> reacts with lithium according to a different mechanism than with sodium. Li<sub>2</sub>S is observed alongside the formation of P-[S]<sub>n</sub>-P intermediates at the SOC of II and prior to the formation of Cu<sup>0</sup> when the cell is fully discharged to 0.8 V. In line with the literature, the P-[S]<sub>n</sub>-P intermediates were found to be redox active according to changes in their relative intensities in the P2*p* spectra for

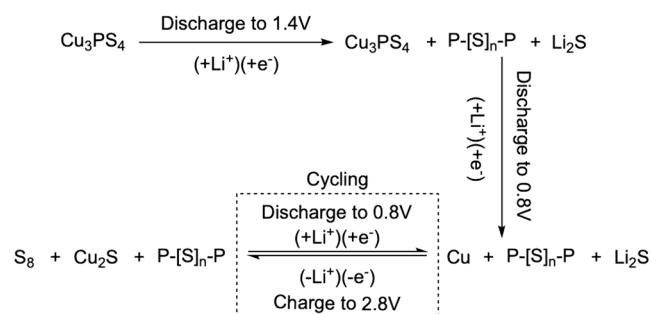
different states of charge.<sup>[21b,34]</sup> At full discharge, Cu<sup>0</sup> was found with residual Cu<sup>+</sup> alongside an increase in Li<sub>2</sub>S. Cu<sup>+</sup> could be reformed during subsequent charge and Li<sub>2</sub>S could also be consumed during this process.

### 3.3.3. Raman Spectroscopy Analysis

Raman spectroscopy was applied to further assign the possible compounds that develop in the electrodes during cycling (see Figure 6b). The  $\beta$ -Li<sub>3</sub>PS<sub>4</sub> Raman spectrum shows a sharp signal at 421 cm<sup>-1</sup> originating from the symmetric stretching mode of the P-S bond in the isolated PS<sub>4</sub><sup>3-</sup>, alongside other smaller bands arising at lower Raman shifts, in accordance with the literature.<sup>[35]</sup> In line with other publications, the ball-milled Cu<sub>3</sub>PS<sub>4</sub> exhibits a strong  $\nu_1$ (A<sub>1</sub>) Raman signal at 389 cm<sup>-1</sup>, along with other  $\nu_1$ (A<sub>1</sub>) and  $\nu_4$ (F<sub>2</sub>) Raman signals that have been algorithmically integrated to form a broad band in the range of 265–335 cm<sup>-1</sup>.<sup>[36]</sup> Hand mixing Cu<sub>3</sub>PS<sub>4</sub>,  $\beta$ -Li<sub>3</sub>PS<sub>4</sub>, and C65 led to the broadening of the major  $\beta$ -Li<sub>3</sub>PS<sub>4</sub> and Cu<sub>3</sub>PS<sub>4</sub> signals in the OCV state (see Figure 6b(I)), which can be attributed to the presence of various P-[S]<sub>n</sub>-P intermediates, as also observed in XPS.<sup>[37]</sup> When discharged to 1.4 V (Figure 6b(II)), an increase in the P-[S]<sub>n</sub>-P Raman signal at 404 cm<sup>-1</sup> can be observed. The Li<sub>2</sub>S Raman signal is expected to show up at 372 cm<sup>-1</sup>,<sup>[38]</sup> but it has low intensity such that it is not visible in our spectra. This is also in line with what has been reported in the literature.<sup>[39]</sup> Nevertheless, the observation of Li<sub>2</sub>S in the XPS confirms its presence. When further discharged to 0.8 V (Figure 6b(III)), primarily signals from  $\beta$ -Li<sub>3</sub>PS<sub>4</sub> are observed. The reduced Cu<sup>0</sup> species is not Raman active. The presence of the  $\beta$ -Li<sub>3</sub>PS<sub>4</sub> signal also helps demonstrate that the Li<sub>2</sub>S formation arises from reaction of Cu<sub>3</sub>PS<sub>4</sub> with Li and the formation of Cu-based P-[S]<sub>n</sub>-P intermediates rather than degradation of  $\beta$ -Li<sub>3</sub>PS<sub>4</sub>. Upon subsequent charging to 2.8 V (Figure 6b (VI)), a signal near the original Cu<sub>3</sub>PS<sub>4</sub>  $\nu_1$ (A<sub>1</sub>) Raman signal arises, but it is shifted to 392 cm<sup>-1</sup>. We know from XPS and XRD that Cu<sub>3</sub>PS<sub>4</sub> does not reform during charge. Therefore, we assign this feature to other P-[S]<sub>n</sub>-P intermediates, and in particular to P<sub>2</sub>S<sub>6</sub><sup>4-</sup>.<sup>[40]</sup> Additionally, two more new peaks located at 219 and 472 cm<sup>-1</sup> were found in the charged sample, which can be attributed to the symmetric S-S bending of S<sub>8</sub> as well as the vibrational stretching mode that results from the covalent S-S bond of S<sub>2</sub> ions in Cu<sub>2</sub>S.<sup>[24b,41]</sup> Through the ex situ Raman study, we further confirmed the presence of S<sub>8</sub> and Cu<sub>2</sub>S accompanied by other P-[S]<sub>n</sub>-P intermediate compounds in the electrode after charging.

### 3.3.4. Proposed Reaction Scheme

Summarizing the previous results, we can propose a reaction mechanism for Cu<sub>3</sub>PS<sub>4</sub> with lithium according to **Scheme 1**. The discharge procedure can be divided into two parts: 1) part of the Cu<sub>3</sub>PS<sub>4</sub> was converted to Li<sub>2</sub>S and P-[S]<sub>n</sub>-P without forming metallic Cu; meanwhile, the primary crystal structure of Cu<sub>3</sub>PS<sub>4</sub> was preserved when the cell was discharged to 1.4 V; 2) along with more lithium taking part in the reaction, the Cu<sub>3</sub>PS<sub>4</sub> was converted to Cu, Li<sub>2</sub>S, and P-[S]<sub>n</sub>-P together with other reaction byproducts after the cell was discharged to



**Scheme 1.** Proposed reaction mechanism (not accounting for proper stoichiometry) for the conversion reaction of  $\text{Cu}_3\text{PS}_4$  in Li solid-state batteries (Li-SSBs).

0.8 V. However, instead of forming  $\text{Cu}_3\text{PS}_4$ , a mixture containing  $\text{S}_8$ ,  $\text{Cu}_2\text{S}$ ,  $\text{P-[S]}_n\text{-P}$ , and other side products were observed after charging. In a nutshell, the pristine  $\text{Cu}_3\text{PS}_4$  converts to a multiphase system, with  $\text{S}_8$ ,  $\text{P-[S]}_n\text{-P}$ , and  $\text{Cu}_2\text{S}$  as redox AMs after the initial cycle. In the following cycles, the newly formed  $\text{S}_8$  and  $\text{Cu}_2\text{S}$  are found to react with lithium at the voltage plateaus around 2.0 V and 1.7 V versus  $\text{Li}^+/\text{Li}$  during lithiation. This second step in the reaction pathway is representative of highly dispersed displacement and conversion mechanisms known in  $\text{Cu}_2\text{S}$ - and  $\text{S}_8$ -based SSBs that are found when the electrolyte is an inorganic ionic conductor.<sup>[42]</sup> This is also in line with the gradual appearance of the step in the voltage profile at around 2 V versus  $\text{Li}^+/\text{Li}$  (see Figure 4), which is close to the values expected for  $\text{S}_8$  redox reactions in Li-S batteries. Influenced by changes in the electrode composition, the electrode and electrolyte interfacial resistance was also found to increase during cycling, as indicated by changes in the medium frequency ( $10^4$ – $10$  Hz) signal in the Nyquist plots shown in Figure S5b, Supporting Information.

## 4. Summary

In summary,  $\text{Cu}_3\text{PS}_4$  was studied as a cathode AM for lithium SSBs. The capacity and cycle life were evaluated for cathode compositions with different ratios of CAM and SE and at different temperatures. The highest capacity was obtained for electrodes containing 40 wt%  $\text{Cu}_3\text{PS}_4$  and cycled at 60 °C. An initial discharge capacity of  $776 \text{ mAh g}^{-1}$  (at  $10 \text{ mA g}^{-1}$ ) was reached which corresponds to 92% of the theoretical capacity ( $843 \text{ mAh g}^{-1}$ ). At  $50 \text{ mA g}^{-1}$ , the capacity is lower, but stable cycling over 60 cycles with capacities close to  $500 \text{ mAh g}^{-1}$  was achieved (59% of the theoretical capacity or  $2.55 \text{ mAh cm}^{-2}$ ). At room temperature, capacities are much lower but still reach values of around  $290 \text{ mAh g}^{-1}$  after 60 cycles ( $50 \text{ mA g}^{-1}$ ). The reaction mechanism is complex, which can be seen from the voltage profiles that exhibit several steps. An emerging plateau at around 2 V indicates that the electrode reaction changes over the course of cycling. Analysis by XRD, XPS, and Raman spectroscopy helped elucidate the complex reaction mechanism. Discharging the cell leads to decomposition of  $\text{Cu}_3\text{PS}_4$  and the formation of an ill-defined phase mixture containing Cu,  $\text{Li}_2\text{S}$ , and  $\text{P-[S]}_n\text{-P}$ .  $\text{Cu}_3\text{PS}_4$  is not reformed during

charging and instead a phase mixture of  $\text{Cu}_2\text{S}$ ,  $\text{S}_8$ , and  $\text{P-[S]}_n\text{-P}$  is found. Based on these analyses and the voltage profiles, the capacity of the electrode is largely dominated by  $\text{Cu}_2\text{S}$  and  $\text{S}_8$  redox processes. The analysis also revealed some differences compared to the same reaction with Na. For Li reacting with  $\text{Cu}_3\text{PS}_4$ , the formation of  $\text{Cu}^0$  starts later as the reaction might proceed over an intermediate phase which does not seem to occur in the case of Na. Overall, the use of ternary compounds such as  $\text{Cu}_3\text{PS}_4$  as conversion-type CAMs seems an interesting strategy to activate various finely dispersed redox centers. Due to the softness of the material, it seems that volume changes are less critical as stable cycling can be achieved. However, a clear bottleneck so far remains the ill-defined voltage profile combined with a large polarization.

## Supporting Information

Supporting Information is available from the Wiley Online Library or from the author.

## Acknowledgements

P.A., K.A.M., and J.J. acknowledge support from the project KAROFEST (grant no. 03XP0498) funded by the Bundesministerium für Bildung und Forschung (BMBF). Z.G.Z. thanks the China Scholarship Council (CSC) for funding. The authors acknowledge Dr. S.L. Mei and Prof. Dr. Y. Lu from the Department of Electrochemical Energy Storage at Helmholtz Zentrum Berlin für Materialien und Energie, GmbH, for assistance with SEM and EDX images.

Open Access funding enabled and organized by Projekt DEAL.

## Conflict of Interest

The authors declare no conflict of interest.

## Data Availability Statement

The data that support the findings of this study are available from the corresponding author upon reasonable request.

## Keywords

conversion reaction,  $\text{Cu}_3\text{PS}_4$ , solid-state batteries, ternary compounds, transition-metal thiophosphate

Received: May 22, 2023

Revised: July 15, 2023

Published online: August 31, 2023

- [1] J. Janek, W. Zeier, *Nat. Energy* **2016**, *1*, 16141.  
 [2] a) R. Koerver, I. Aygün, T. Leichtweiß, C. Dietrich, W. Zhang, J. O. Binder, P. Hartmann, W. G. Zeier, J. Janek, *Chem. Mater.* **2017**, *29*, 5574; b) T. Shi, Y.-Q. Zhang, Q. Tu, Y. Wang, M. C. Scott, G. Ceder, *J. Mater. Chem. A* **2020**, *8*, 17399; c) X. Wu, J. Billaud, I. Jerjen, F. Marone, Y. Ishihara, M. Adachi, Y. Adachi, C. Villevieille, Y. Kato, *Adv. Energy Mater.* **2019**, *9*, 1901547; d) S. Lou, Z. Yu, Q. Liu, H. Wang, M. Chen, J. Wang, *Chemistry* **2020**, *6*, 2199; e) Y. Zhu, X. He, Y. Mo, *ACS Appl Mater*

- Interfaces* **2015**, *7*, 23685; f) G. F. Dewald, S. Ohno, M. A. Kraft, R. Koerver, P. Till, N. M. Vargas-Barbosa, J. Janek, W. G. Zeier, *Chem. Mater.* **2019**, *31*, 8328.
- [3] a) N. Kamaya, K. Homma, Y. Yamakawa, M. Hirayama, R. Kanno, M. Yonemura, T. Kamiyama, Y. Kato, S. Hama, K. Kawamoto, A. Mitsui, *Nat. Mater.* **2011**, *10*, 682; b) H. Yamane, M. Shibata, Y. Shimane, T. Junke, Y. Seino, S. Adams, K. Minami, A. Hayashi, M. Tatsumisago, *Solid State Ionics* **2007**, *178*, 1163; c) L. L. Baranowski, C. M. Heveran, V. L. Ferguson, C. R. Stoldt, *ACS Appl. Mater. Interfaces* **2016**, *8*, 29573; d) H. Stöffler, T. Zinkevich, M. Yavuz, A.-L. Hansen, M. Knapp, J. Bednarčík, S. Randau, F. H. Richter, J. Janek, H. Ehrenberg, S. Indris, *J. Phys. Chem. C* **2019**, *123*, 10280; e) Z. Liu, W. Fu, E. A. Payzant, X. Yu, Z. Wu, N. J. Dudney, J. Kiggans, K. Hong, A. J. Rondinone, C. Liang, *J. Am. Chem. Soc.* **2013**, *135*, 975.
- [4] a) P. Minnmann, F. Strauss, A. Bielefeld, R. Ruess, P. Adelhelm, S. Burkhardt, S. L. Dreyer, E. Trevisanello, H. Ehrenberg, T. Brezesinski, F. H. Richter, J. Janek, *Adv. Energy Mater.* **2022**, *12*, 2201425; b) T.-T. Zuo, F. Walther, S. Ahmed, R. Rueß, J. Hertle, B. Mogwitz, K. Volz, J. Janek, *ACS Energy Lett.* **2023**, *8*, 1322; c) N. Ahmad, S. Sun, P. Yu, W. Yang, *Adv. Funct. Mater.* **2022**, *32*, 2201528.
- [5] a) F. Klein, B. Jache, A. Bhide, P. Adelhelm, *Phys. Chem. Chem. Phys.* **2013**, *15*, 15876; b) J. Cabana, L. Monconduit, D. Larcher, M. R. Palacin, *Adv. Mater.* **2010**, *22*, E170.
- [6] S. Ohno, W. G. Zeier, *Acc. Mater. Res.* **2021**, *2*, 869.
- [7] D. H. Tan, Y.-T. Chen, H. Yang, W. Bao, B. Sreenarayanan, J.-M. Doux, W. Li, B. Lu, S.-Y. Ham, B. Sayahpour, J. Scharf, E. A. Wu, G. Deysher, H. E. Han, H. J. Hah, H. Jeong, J. B. Lee, Z. Chen, Y. S. Meng, *Science* **2021**, *373*, 1494.
- [8] A. L. Santhosha, L. Medenbach, J. R. Buchheim, P. Adelhelm, *Batteries Supercaps* **2019**, *2*, 524.
- [9] T. Palaniselvam, A. I. Freytag, H. Moon, K. A. Janßen, S. Passerini, P. Adelhelm, *J. Phys. Chem. C* **2022**, *126*, 13043.
- [10] A. Hayashi, A. Inoue, M. Tatsumisago, *J. Power Sources* **2009**, *189*, 669.
- [11] A. Ueda, M. Nagao, A. Inoue, A. Hayashi, Y. Seino, T. Ota, M. Tatsumisago, *J. Power Sources* **2013**, *244*, 597.
- [12] J. M. Whiteley, S. Hafner, S. S. Han, S. C. Kim, K. H. Oh, S.-H. Lee, *Adv. Energy Mater.* **2016**, *6*, 1600495.
- [13] X. Yao, D. Liu, C. Wang, P. Long, G. Peng, Y. S. Hu, H. Li, L. Chen, X. Xu, *Nano. Lett.* **2016**, *16*, 7148.
- [14] A. L. Santhosha, P. K. Nayak, K. Pollok, F. Langenhorst, P. Adelhelm, *J. Phys. Chem. C* **2019**, *123*, 12126.
- [15] a) S. M. Hosseini, A. Varzi, S. Ito, Y. Aihara, S. Passerini, *Energy Storage Mater.* **2020**, *27*, 61; b) A. L. Santhosha, N. Nazer, R. Koerver, S. Randau, F. H. Richter, D. A. Weber, J. Kulisch, T. Adermann, J. Janek, P. Adelhelm, *Adv. Energy Mater.* **2020**, *10*, 2002394; c) Z. Zhang, K. Dong, K. A. Mazzi, A. Hilger, H. Markötter, F. Wilde, T. Heinemann, I. Manke, P. Adelhelm, *Adv. Energy Mater.* **2023**, *13*, 2203143.
- [16] Y. Fujii, A. Miura, N. C. Rosero-Navarro, M. Higuchi, K. Tadanaga, *Electrochim. Acta* **2017**, *241*, 370.
- [17] W. Brehm, A. L. Santhosha, Z. Zhang, C. Neumann, A. Turchanin, A. Martin, N. Pinna, M. Seyring, M. Rettenmayr, J. R. Buchheim, P. Adelhelm, *Adv. Funct. Mater.* **2020**, *30*, 1910583.
- [18] Y. Fujii, A. Miura, N. C. Rosero-Navarro, Y. Mizuguchi, C. Moriyoshi, Y. Kuroiwa, M. Higuchi, K. Tadanaga, *J. Electrochem. Soc.* **2018**, *165*, A2948.
- [19] a) X. Yin, Y. Ren, L. Wu, Z. Zhang, C. Du, J. Wang, G. Yin, H. Huo, *J. Energy Chem.* **2022**, *71*, 210; b) T. A. Yersak, H. A. Macpherson, S. C. Kim, V.-D. Le, C. S. Kang, S.-B. Son, Y.-H. Kim, J. E. Trevey, K. H. Oh, C. Stoldt, S.-H. Lee, *Adv. Energy Mater.* **2013**, *3*, 120.
- [20] X. Sun, A. M. Stavola, D. Cao, A. M. Bruck, Y. Wang, Y. Zhang, P. Luan, J. W. Gallaway, H. Zhu, *Adv. Energy Mater.* **2020**, *11*, 2002861.
- [21] a) T. Swamy, X. Chen, Y.-M. Chiang, *Chem. Mater.* **2019**, *31*, 707; b) T. Hakari, M. Deguchi, K. Mitsuhashi, T. Ohta, K. Saito, Y. Orikasa, Y. Uchimoto, Y. Kowada, A. Hayashi, M. Tatsumisago, *Chem. Mater.* **2017**, *29*, 4768; c) T. Hakari, M. Nagao, A. Hayashi, M. Tatsumisago, *Solid State Ionics* **2014**, *262*, 147.
- [22] T. Takeuchi, H. Kageyama, K. Nakanishi, M. Ogawa, T. Ohta, A. Sakuda, H. Sakaebe, H. Kobayashi, Z. Ogumi, *J. Electrochem. Soc.* **2015**, *162*, A1745.
- [23] Z. Xu, R. Chen, H. Zhu, *J. Mater. Chem. A* **2019**, *7*, 12645.
- [24] a) Y. Son, J.-S. Lee, Y. Son, J.-H. Jang, J. Cho, *Adv. Energy Mater.* **2015**, *5*, 1500110; b) L. Medenbach, I. Escher, N. Kowitsch, M. Armbruster, L. Zedler, B. Dietzek, P. Adelhelm, *Angew. Chem. Int. Ed.* **2018**, *57*, 13666; c) A. Hayashi, T. Ohtomo, F. Mizuno, K. Tadanaga, M. Tatsumisago, *Electrochim. Acta.* **2004**, *50*, 893; d) J. Auvergniot, A. Cassel, J.-B. Ledeuil, V. Viallet, V. Seznec, R. Dedryvère, *Chem. Mater.* **2017**, *29*, 3883.
- [25] a) R. Koerver, F. Walther, I. Aygün, J. Sann, C. Dietrich, W. G. Zeier, J. Janek, *J. Mater. Chem. A* **2017**, *5*, 22750; b) F. Walther, S. Randau, Y. Schneider, J. Sann, M. Rohnke, F. H. Richter, W. G. Zeier, J. Janek, *Chem. Mater.* **2020**, *32*, 6123.
- [26] S. K. Otto, L. M. Riegger, T. Fuchs, S. Kayser, P. Schweitzer, S. Burkhardt, A. Henss, J. Janek, *Adv. Mater. Interfaces* **2022**, *9*, 2102387.
- [27] a) X. Li, J. Liang, M. N. Bani, J. Luo, C. Wang, W. Li, X. Li, Q. Sun, Y. Hu, Q. Xiao, T.-K. Sham, L. Zhang, S. Zhao, S. Lu, H. Huang, R. Li, X. Sun, *Energy Storage Mater.* **2020**, *28*, 325; b) D. H. S. Tan, E. A. Wu, H. Nguyen, Z. Chen, M. A. T. Marple, J.-M. Doux, X. Wang, H. Yang, A. Banerjee, Y. S. Meng, *ACS Energy Lett.* **2019**, *4*, 2418.
- [28] F. Walther, R. Koerver, T. Fuchs, S. Ohno, J. Sann, M. Rohnke, W. G. Zeier, J. Janek, *Chem. Mater.* **2019**, *31*, 3745.
- [29] a) Y. Su, L. Ye, W. Fitzhugh, Y. Wang, E. Gil-González, I. Kim, X. Li, *Energy Environ. Sci.* **2020**, *13*, 908; b) Z. Liu, A. Borodin, G. Li, X. Liu, Y. Li, F. Endres, *J. Phys. Chem. C* **2019**, *124*, 300; c) K. N. Wood, K. X. Steirer, S. E. Hafner, C. Ban, S. Santhanagopalan, S. H. Lee, G. Teeter, *Nat. Commun.* **2018**, *9*, 2490.
- [30] M. Fantauzzi, B. Elsener, D. Atzei, A. Rigoldi, A. Rossi, *RSC Adv.* **2015**, *5*, 75953.
- [31] a) Y. Ma, J. H. Teo, F. Walther, Y. Ma, R. Zhang, A. Mazilkin, Y. Tang, D. Goonetilleke, J. Janek, M. Bianchini, T. Brezesinski, *Adv. Funct. Mater.* **2022**, *32*, 2111829; b) J. H. Teo, F. Strauss, F. Walther, Y. Ma, S. Payandeh, T. Scherer, M. Bianchini, J. Janek, T. Brezesinski, *Mater. Futures* **2022**, *1*, 015102.
- [32] a) M. Fantauzzi, D. Atzei, B. Elsener, P. Lattanzi, A. Rossi, *Surf. Interface Anal.* **2006**, *38*, 922; b) V. I. Nefedov, Y. V. Salyn, E. P. Domashevskaya, Y. A. Ugai, V. A. Terekhov, *J. Electron Spectrosc. Relat. Phenom.* **1975**, *6*, 231.
- [33] a) Y. Mikhlin, V. Nasluzov, Y. Tomashevich, S. Vorobyev, A. Romanchenko, M. Likhatski, *Faraday Discuss.* **2022**, *236*, 205; b) V. Nasluzov, A. Shor, A. Romanchenko, Y. Tomashevich, Y. Mikhlin, *J. Phys. Chem. C* **2019**, *123*, 21031.
- [34] S. Wang, M. Tang, Q. Zhang, B. Li, S. Ohno, F. Walther, R. Pan, X. Xu, C. Xin, W. Zhang, L. Li, Y. Shen, F. H. Richter, J. Janek, C. W. Nan, *Adv. Energy Mater.* **2021**, *11*, 2101370.
- [35] T. Yamada, S. Ito, R. Omoda, T. Watanabe, Y. Aihara, M. Agostini, U. Ulissi, J. Hassoun, B. Scrosati, *J. Electrochem. Soc.* **2015**, *162*, A646.
- [36] a) J. Shamir, S. Fiechter, H. Wetzel, *J. Raman Spectrosc.* **1986**, *17*, 217; b) B. Graeser, R. Agrawal, *RSC Adv.* **2018**, *8*, 34094.
- [37] a) C. Dietrich, D. A. Weber, S. Culver, A. Senyshyn, S. J. Sedlmaier, S. Indris, J. Janek, W. G. Zeier, *Inorg. Chem.* **2017**, *56*, 6681; b) M. Tachez, J. P. Malugani, R. Mercier, G. Robert, *Solid State Ionics* **1984**, *14*, 181; c) Y. Aoki, K. Ogawa, T. Nakagawa,

- Y. Hasegawa, Y. Sakiyama, T. Kojima, M. Tabuchi, *Solid State Ionics* **2017**, *310*, 50.
- [38] Z. W. Seh, H. Wang, P.-C. Hsu, Q. Zhang, W. Li, G. Zheng, H. Yao, Y. Cui, *Energy Environ. Sci.* **2014**, *7*, 672.
- [39] a) W. Zhu, A. Paoletta, C. S. Kim, D. Liu, Z. Feng, C. Gagnon, J. Trottier, A. Vijn, A. Guerfi, A. Mauger, C. M. Julien, M. Armand, K. Zaghbi, *Sustainable Energy Fuels* **2017**, *1*, 737; b) J.-T. Yeon, J.-Y. Jang, J.-G. Han, J. Cho, K. T. Lee, N.-S. Choi, *J. Electrochem. Soc.* **2012**, *159*, A1308; c) E. Nagai, T. S. Arthur, P. Bonnick, K. Suto, J. Muldoon, *MRS Adv.* **2019**, *4*, 2627.
- [40] C. Dietrich, D. A. Weber, S. J. Sedlmaier, S. Indris, S. P. Culver, D. Walter, J. Janek, W. G. Zeier, *J. Mater. Chem. A* **2017**, *5*, 18111.
- [41] a) Y. Zuo, Y. Liu, J. Li, R. Du, X. Han, T. Zhang, J. Arbiol, N. J. Divins, J. Llorca, N. Guijarro, K. Sivula, A. Cabot, *Chem. Mater.* **2019**, *31*, 7732; b) S. Cabrini, G. Léronde, A. M. Schwartzberg, T. Mokari, S.-Y. Fu, H.-H. Chang, Y.-K. Hsu, Y.-G. Lin, *Nanophotonic Mater. XI* **2014**, *9161*, 25
- [42] a) Y. Wang, X. Feng, Y. Xiong, S. Stoupin, R. Huang, M. Zhao, M. Xu, P. Zhang, J. Zhao, H. D. Abruña, *ACS Appl. Mater. Interfaces* **2020**, *12*, 17396; b) T. Yamada, S. Ito, R. Omoda, T. Watanabe, Y. Aihara, M. Agostini, U. Ulissi, J. Hassoun, B. Scrosati, *J. Electrochem. Soc.* **2015**, *162*, A646; c) H. Kim, J. T. Lee, A. Magasinski, K. Zhao, Y. Liu, G. Yushin, *Adv. Energy Mater.* **2015**, *5*, 1501306; d) Z. Yang, Z. Zhu, J. Ma, D. Xiao, X. Kui, Y. Yao, R. Yu, X. Wei, L. Gu, Y.-S. Hu, H. Li, X. Zhang, *Adv. Energy Mater.* **2016**, *6*, 1600806.